Electronic Supplementary Information For:

High Performance Inkjet Printed Embedded Electrochemical Sensors for Monitoring Hypoxia in Gut Bilayer Microfluidic Chip

*Muhammad Asad Ullah Khalid[1,†], Kyung Hwan Kim[1,†], Abdul Rahim Chethikkattuveli Salih[1], Kinam Hyun[1], Sung Hyuk Park[1], Bohye Kang[1], Afaque Manzoor Soomro[1], Muhsin Ali[1], Yesl Jun[2], Dongeun Huh[3], Heeyeong Cho[2,**], Kyung Hyun Choi[1,*]*

[1]Department of Mechatronics Engineering, Jeju National University, Republic of Korea
[2]Center for Bio Platform Technology, Bio & Drug Discovery Division, Korea Research Institute of Chemical technology
[3]Department of Bioengineering, University of Pennsylvania, Philadelphia, USA

[†]*Muhammad Asad Ullah Khalid and Kyung Hwan Kim* contributed equally to this manuscript.

*Corresponding Author

*E-mail: amm@jejunu.ac.kr

*Phone: +82-64-754-3713

*Fax: +82-64-752-3174

**Co-corresponding Author

**E-mail: hycho@krict.re.kr

**Phone number: +10-8641-6402

ECM Coating Protocol

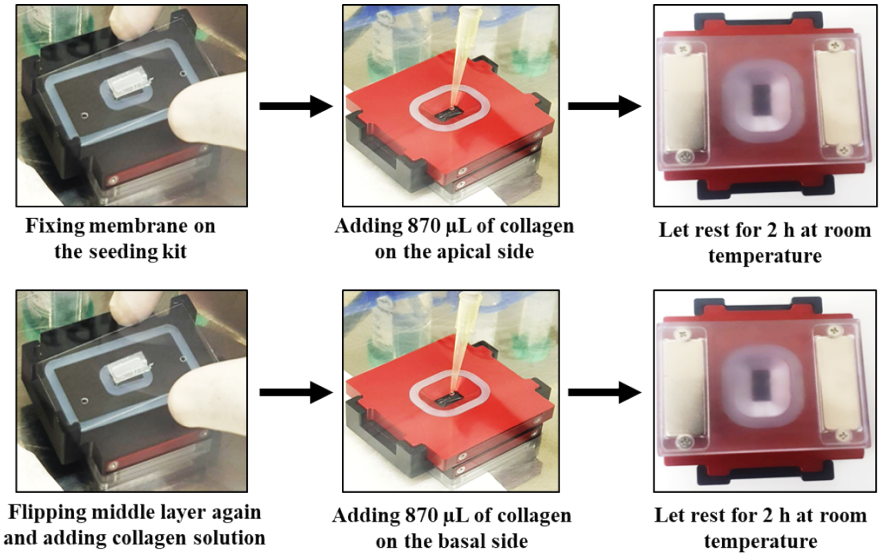

Figure S1. Step by step approach for ECM coating is shown. It is ensured that collagen solution touches the membrane followed by the removal of the collagen solution from both sides and washing with the PBS after incubating each side. Both sides are again filled with collagen solution and overnight incubated at 4 ^{o}C followed by emptying both sides and washing with PBS again.

Cell Seeding Protocol

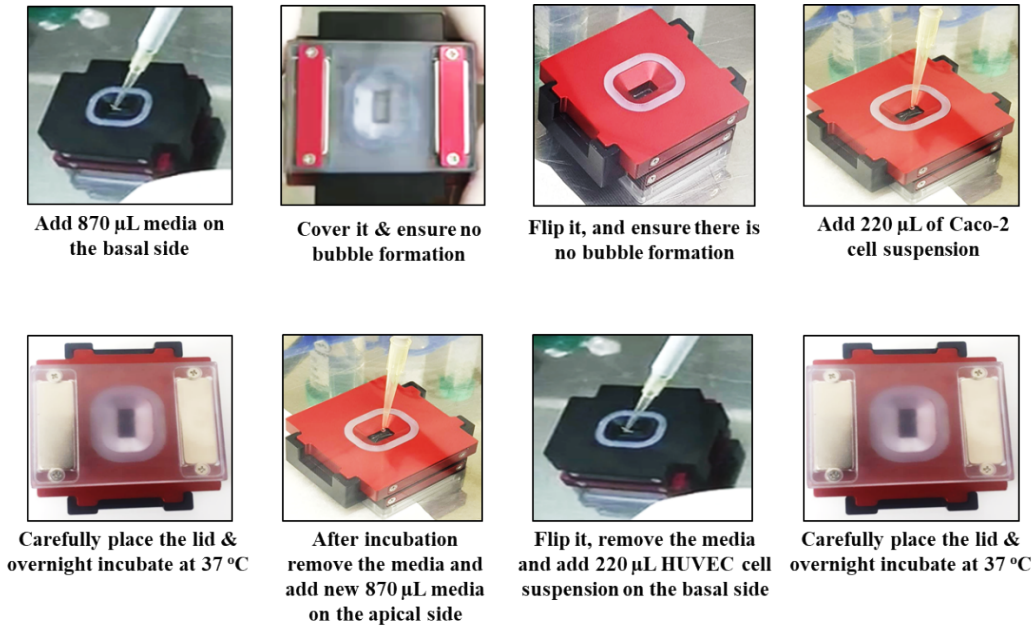

Figure S2. Cell seeding protocol, which was followed, has been shown. After following the above mentioned steps, media is removed and tissue is washed with the PBS. Middle bilayer tissue part is ready to be assembled with top and bottom glass for the microfluidic experiments.

Interfacing Front-end Circuits

TEEI Measuring Circuit Schematic

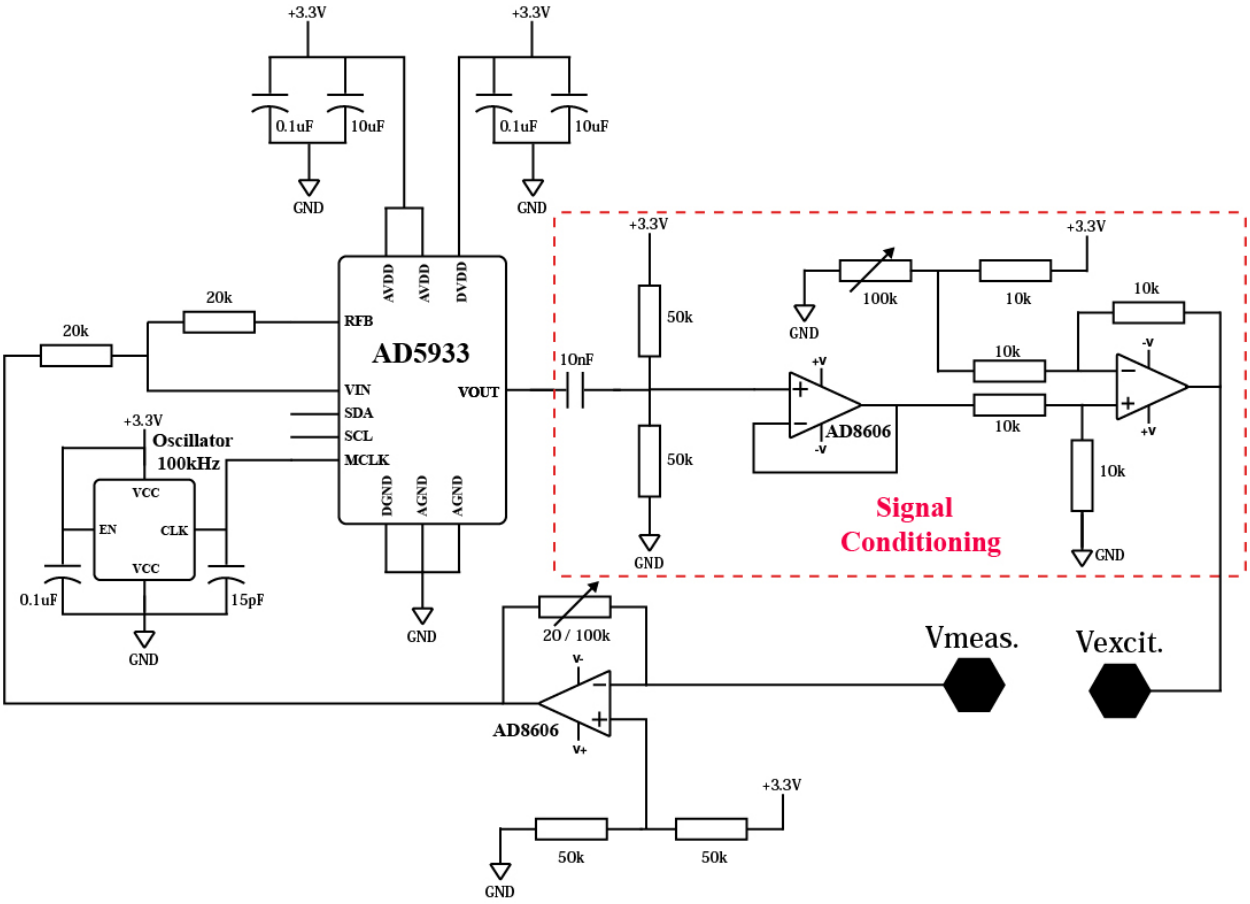

Chronoamperometric Measurements' Circuit Schematic

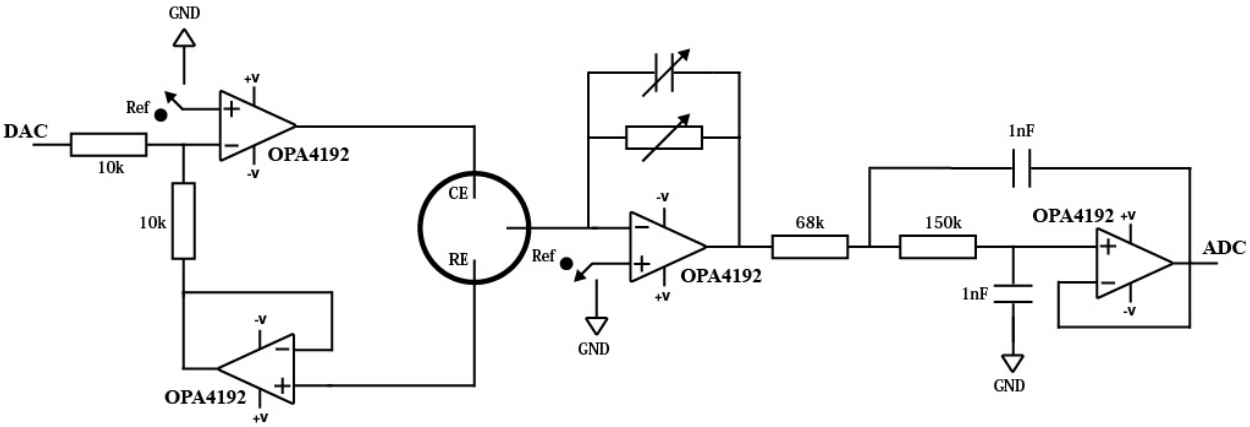

Figure S3. An AD5933 impedance analyzer was used for making a measurement unit for TEEI.

Whereas, a potentiostat circuit was developed for chronoamperometric measurements of three-electrode DO and ROS sensors. The printed circuit boards (PCBs) were designed in “Autodesk Eagle” and fabricated for use as sensor analog interfaces in the systems.

a

b

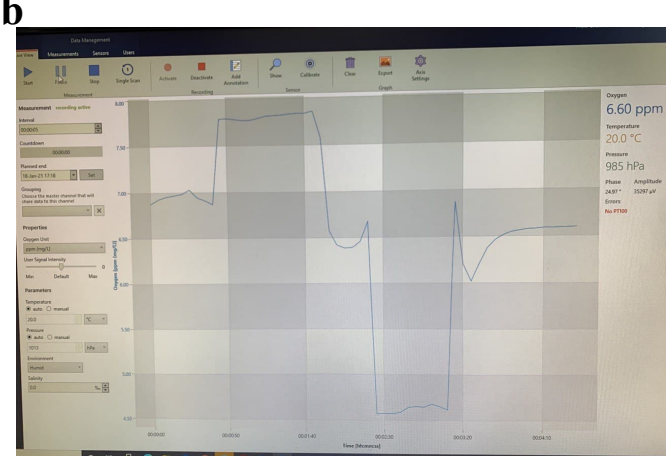

Figure S4. Sample Solutions for DO sensor characterizations and calibration: **(a)** Na_2SO_4 in PBS; **(b)** Commercial DO sensor software (screenshot) used for preparing standardized samples of DO as shown in (a).

Figure S5. A snapshot of the data acquisition software showing the data for epithelium side DO sensors connected to the system. The change in output signal is because of the two different locations of DO sensors which shows the consumption of dissolved oxygen by Caco-2 epithelium in real time.

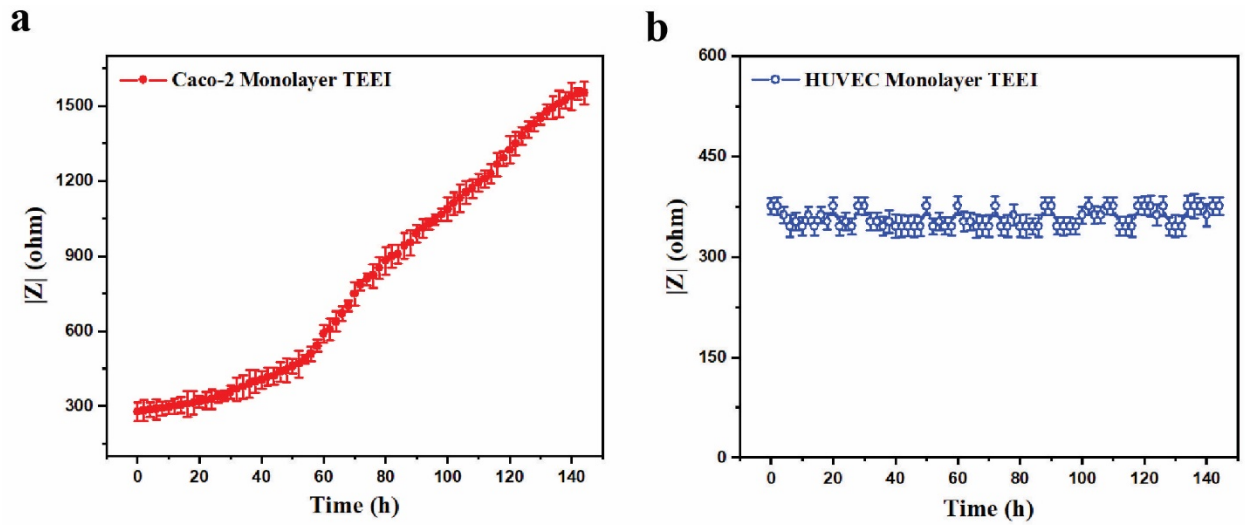

Figure S6. TEEI values of monolayer tissues: **(a)** Caco-2, and **(b)** HUVECs, measured using custom developed impedance measurement unit at excitation signal frequency of 60Hz with a time interval of 2 h for 6 days, n = 3. As can be seen that in a monolayer TEEI measuring chip the Caco-2 epithelial cells show increasing impedance values, hence, cell index (CI), whereas, in endothelial HUVEC monolayer the TEEI change was negligible in comparison.

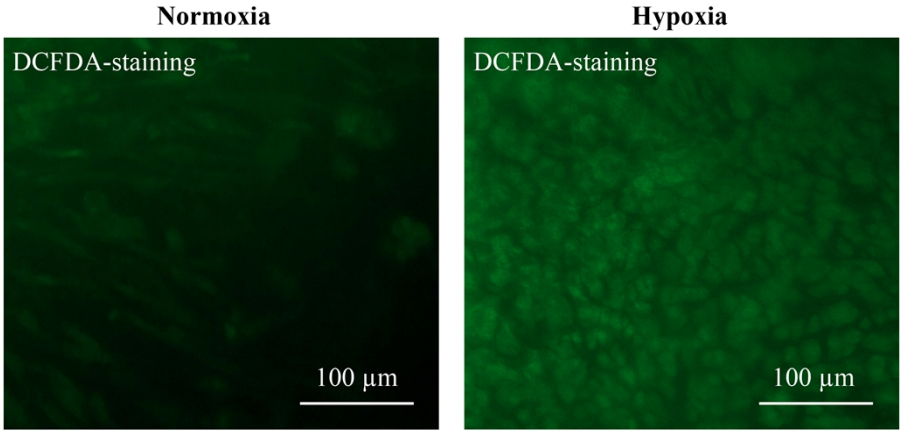

Figure S7. DCFDA (ROS) staining images of Caco-2 showing higher expression in hypoxia as compared to normoxia.

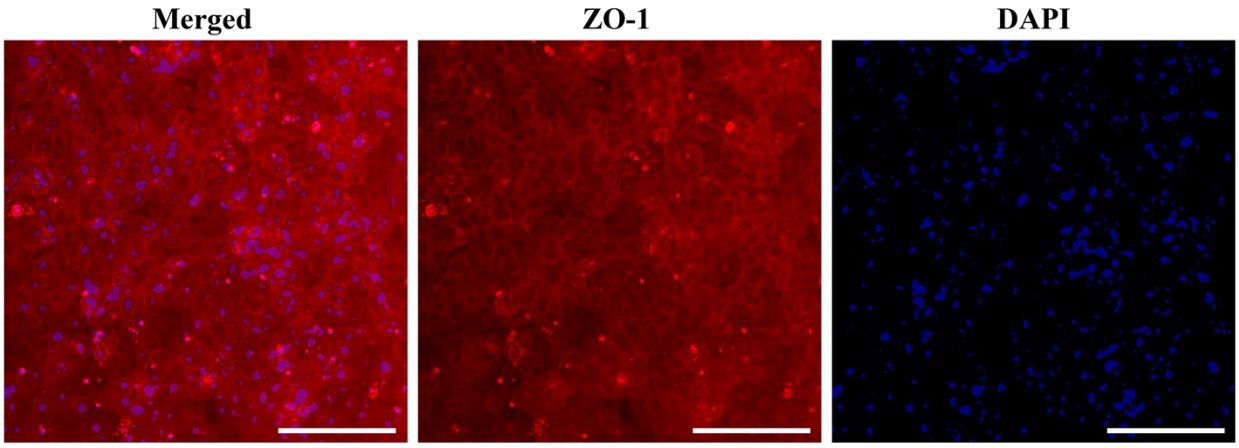

Figure S8. ZO-1 staining images of HUVEC showing the tight junctions which remained same over longer period of time.

Table. S1. A comparison of gut in-vitro platforms using Caco-2 cell line.

Gut in vitro Model	Barrier Permeability	Integrated Monitoring	Oxygen Control	Application	Reference
Monolayer	No	TEER	No	Barrier Integrity	[1]
Monolayer	Lucifer Yellow	No	No	Oral Bioavailability	[2]
Monolayer	Omeprazole, Verapamil	No	No	Oral Bioavailability	[3]
Monolayer	Caffeine and Atenolol	No	No	Chemotherapeutics Screening	[4]
Monolayer	Lucifer Yellow	Flow Sensors	No	Drug Transport	[5]
Monolayer (Transwell)	4-kDa FITC-dextran	TEER	Yes	Barrier Assessment	[6]
3D Villi (Scaffold)	Fluorescein, Rhodamine 123	No	No	Improve in-vitro Physiology	[7]
Co-culture (Porous Membrane)	4 kDa fluorescein isothiocyanate-conjugated dextran	DO and TEER	Yes	human–microbe interface	[8]
Bilayer co-culture (Porous Membrane)	Cascade blue 5.9 kDa	DO Sensors	Yes	Host microbe interactions	[9]
Intestinal Tubes (Membrane Free)	150 kDa FITC-dextran, 4.4 kDa TRITC-dextran	No	No	Barrier Assessment	[10]
Bilayer co-culture (Porous Membrane)	Dextran 40 kDa MW	DO, ROS and TEEI Sensors	Yes	Barrier Assessment	This Work

Computational fluid dynamics for gut bilayer development

"Laminar fluid flow" and "Transport of diluted species" in the GI barrier was simulated using "*COMSOL Multiphysics 5.6"*. Laminar fluid flow was governed by the Navier-Stokes equations and dilute species (Daxtran) transport by the advection-diffusion equation, both solved in COMSOL, subject to the following boundary conditions: No-slip on all media channel walls and membrane surfaces; laminar inflow rate specified at the media channels inlet; laminar outflow conditions at the outlet; dilute species concentration specified at inlet of upper channel. In simulations, fluid (media with supplements) model with a density of 1000 kg/m^3 and a dynamic viscosity of 0.89 mPa.s at 37°C was used. Flow across the 20-μm thick porous membrane was neglected, and cultured cells on the cell chamber side of the membrane resulted in flow resistances through the membrane that were orders of magnitude higher than through the media channel (height 300 μm). Moreover, the cultured cells within the cell chamber increased flow resistance there. Two sets of COMSOL simulations were conducted. In the first set, the transport of a generic small molecule within culture media in the GI was modeled with inlet flow rates of 6 μL/min, 12.5 μl/min and 25 μl/min, an inlet concentration of 0.2 mol/m^3, zero initial concentration in the device, a diffusion coefficient of 1.0×10^{-9} m^2/s in culture media and no cell uptake and no flux through walls. The media channel inlet, initial media channel and cell chamber daxtran concentrations were 0.2 mol/m^3, which is the saturation level in culture media at 37°C in equilibrium with ambient incubator air at 37°C, and 1 atm pressure. Diffusion coefficients of daxtran [11] in culture media was 44 $\mu m^2/s$ for dextran 38400 MW, however, a higher value of 4400 $\mu m^2/s$ was chosen, due to possible higher MW and gravitation effects. A cell density in the cell chamber of $\rho cell = 2 \times 10^5$ cells/mL was assumed per GI barrier chip.

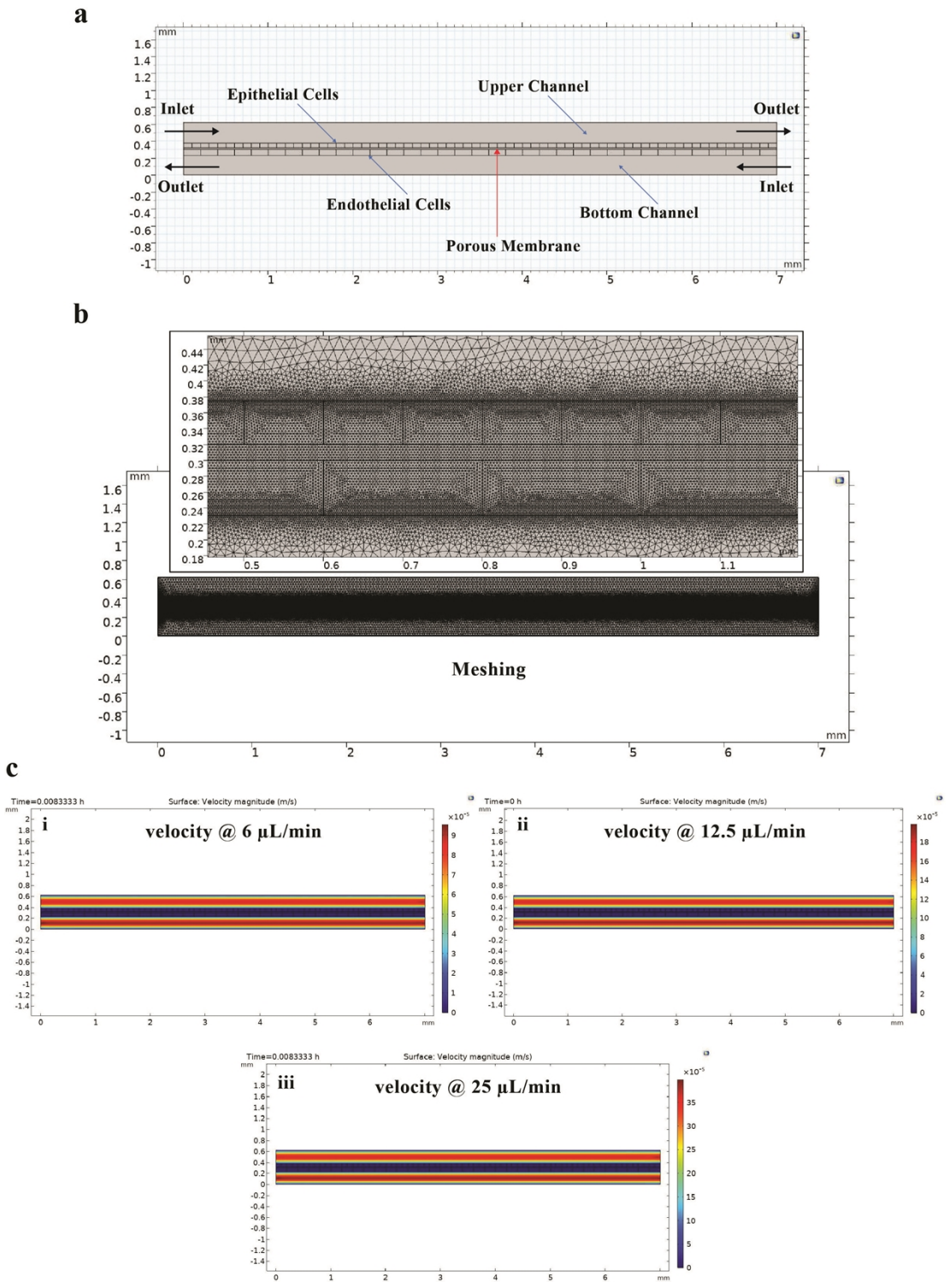

Figure S9. CFD simulation model characteristics: **(a)** geometry of cell culture chamber with cells on top and bottom surface of a porous membrane - designating model parameters, **(b)** gut

on chip barrier meshing in the simulation model, **(b)** surface velocity magnitudes at different flow rates.

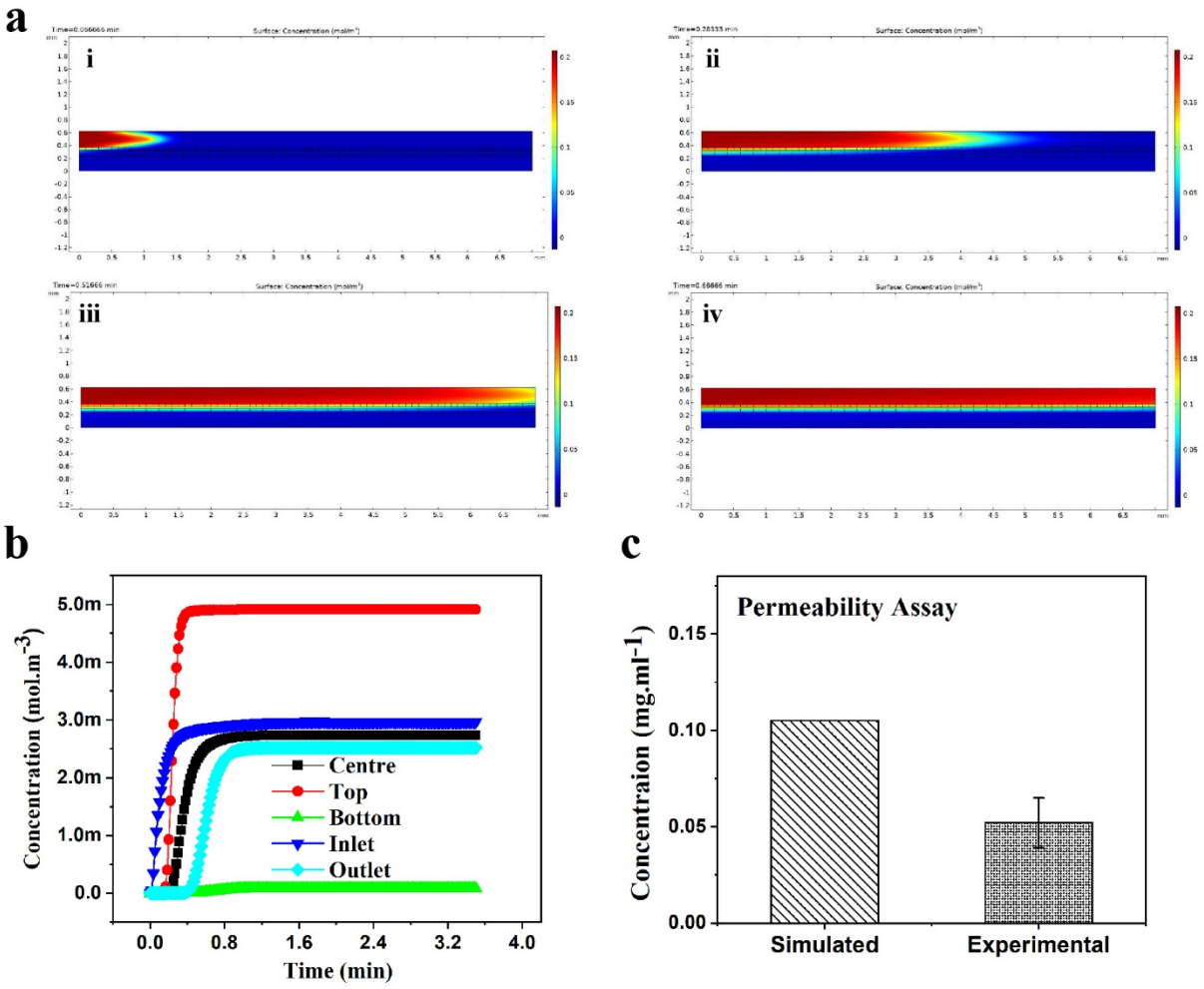

Figure S10. Gut barrier permeability simulated and experimental response: **(a)** CFD – 2D simulation contour plots for gut barrier in bilayer chip device showing surface concentrations for dextran 40000 MW at different time points: i = 0.067min, ii = 0.283min, iii = 0.517min, iv = 0.667min, **(b)** plot for surface concentration at different points of interest in bilayer chip **(c)** permeability assay comparison plot where experimental concentration is (0.052 $mg.mL^{-1}$ ± 0.013) less than simulated value (0.103 $mg.mL^{-1}$), n = 3, value = mean ± sd.

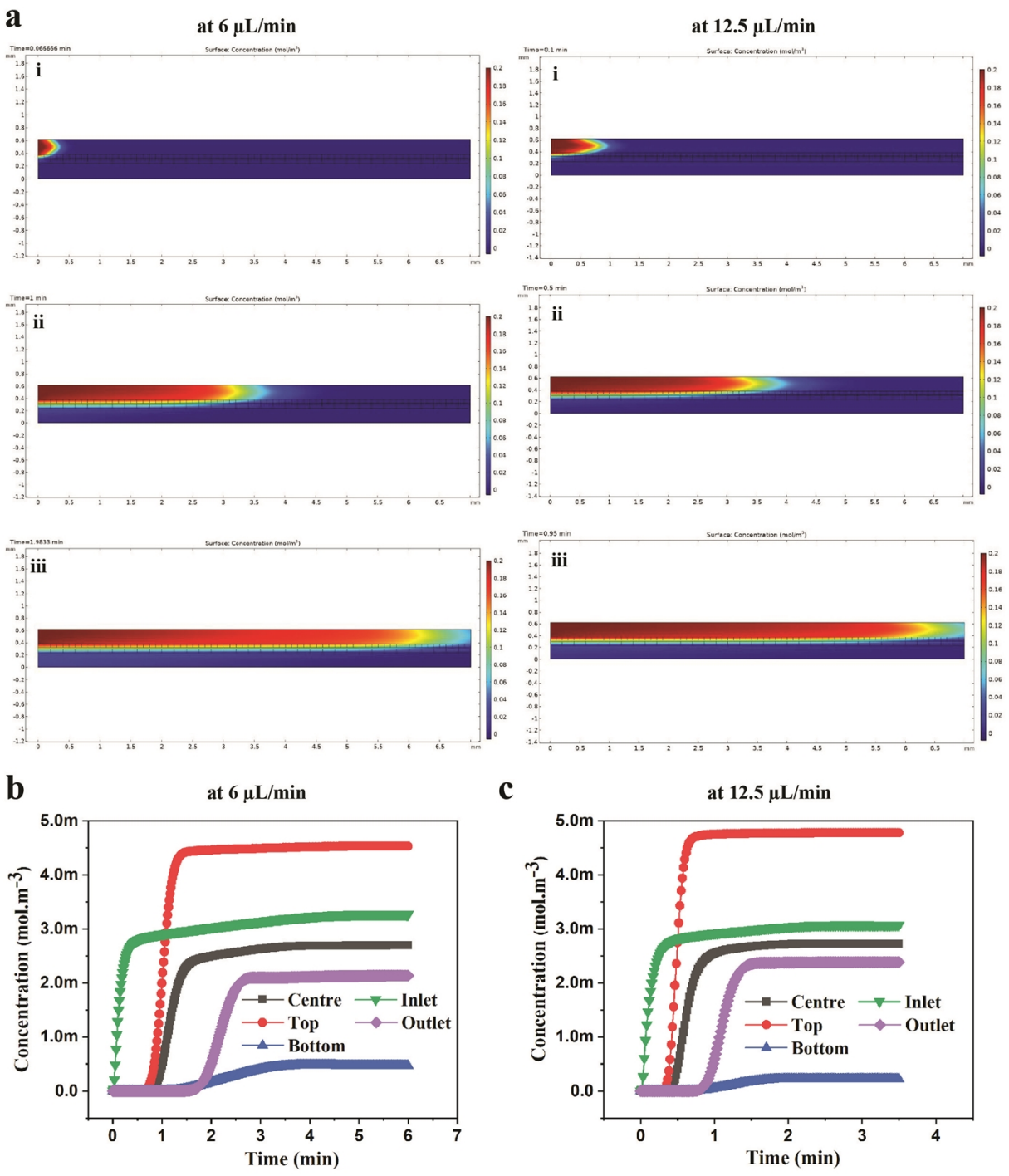

Figure S11. CFD simulation results: **(a)** contour plots for 6 µL/min flow rate at different time points i = 0.67 min, ii = 1 min, iii = 1.98 min, & contour plots for 12.5 µL/min flow rate at different time points i = 0.1 min, ii = 0.5 min, iii = 0.95 min, **(b)** surface concentration change

with time plots at different point locations 6 µL/min flow rate, **(c)** surface concentration change with time plots at different point locations 12.5 µL/min flow rate.

The COMSOL Multiphysics® model for GI barrier comprises glass slab containing upper and lower media channels in the cell chamber, separated by a porous membrane (**Figure S9a)**. By symmetry about the vertical and horizontal center plane, the computational domain was chosen to be 2D side view of the cell chamber area. Model setup of cell chamber, upper and lower media channel, and membrane portions of computational domain are shown in **Figure S9a**. The heights of upper and lower media channels in the cell chamber were 300 µm and the membrane thickness was 9 µm. Flow enters the inlet at 12.5 µL/min and exits at the outlet of each media channel in opposite directions. Laminar inflow and outflow conditions were used in COMSOL Multiphysics®. The membrane was modeled as a 2D planar surface between the upper and lower media channel in the cell chamber, with effective diffusivities for Dextran and small molecules. Fluid flow across the membrane was neglected, and constant flow velocity at predetermined flow rates (6, 12.5 and 25 µL/min) was assumed throughout the cell chamber. No-slip conditions were imposed at all chamber walls, cell walls and membrane surfaces within the cell chamber. For dextran transport simulations, cells were assumed to fill the cell chamber volume at a specified density and consume dextran at a specified rate (see main text for details). GI barrier model mesh of the cell chamber, cells, and membrane portions of computational domain are shown in **Figure S9b**. Triangular mesh elements were used at all surfaces and mesh density was kept higher near the cells and membrane area due to low size and thickness of cells and membrane. Mesh sensitivity analysis was performed to show that this mesh resolution yields sufficiently accurate numerical results. Triangular finite elements were used for the flow velocity components, fluid pressure, and species concentration. For shear stress calculations on the cells and membrane at 6, 12.5 and 25 µL/min flow rates, no-slip conditions were assumed at all walls as well as along the membrane (**Figure S9)**. Dextran saturation in cell chamber was determined at 7 min for a flow rate of 6, 12.5 and 25 µL/min. (**Figure S10 and Figure S11)**.

The flow magnitude in the chamber is governed by the Navier-Stokes equations in the “Laminar Fluid Flow” Module in COMSOL.

$$\rho\frac{\partial u}{\partial t} + \rho(u \cdot \nabla)u = \nabla \cdot [-pI + K] + F \qquad \textbf{(eq. S1)}$$

Where **u** is the fluid velocity, **p** is the fluid pressure, **ρ** is the fluid density,

The different terms correspond to the inertial forces (Left hand side), pressure forces, viscous forces, and the external forces applied to the fluid (Right hand side).

These equations are always solved simultaneously with continuity equation:

$$\frac{\partial \rho}{\partial t} + \nabla(\rho u) = 0 \qquad \textbf{(eq. S2)}$$

Equation (2) for an incompressible fluid under steady state conditions reduces to:

$$\rho \nabla \cdot u = 0 \qquad \textbf{(eq. S3)}$$

The Navier-Stokes equations represent the conservation of momentum, while the continuity equation represents the conservation of mass for the solution (Media and dissolved tracer).

The concentration profiles are determined by diffusion and convection as described in the following PDE in the "Transport of diluted species" module.

$$\frac{\partial(\in_p c_i)}{\partial_t} + \frac{\partial(\rho c_{Pj})}{\partial_t} + \nabla \cdot J_i + u \cdot \nabla c_i = R_i + S_i \qquad \textbf{(eq. S4)}$$

$$\text{Where } J_i = -(D_{Dj} + D_{ej})\nabla c_i \qquad \textbf{(eq. S5)}$$

"c" is the concentration of the species (mol/m^3), D denotes the diffusion coefficient (m^2/s), R is a reaction rate expression for the species (mol/(m^3·s)), **u** is the velocity vector (m/s).

The first term on the left-hand side of Equation (4) corresponds to the accumulation of the species. The third term accounts for the convective transport due to a velocity field **u**. This field can be expressed analytically or be obtained from coupling this physics interface to one that describes fluid flow (momentum balance). To include convection in the mass balance equation, an expression that includes the space and time variables, or the velocity vector component variable names from a fluid flow physics interface of COMSOL, can be entered into the appropriate field. The velocity fields from existing fluid flow interfaces are available directly as predefined fields (model inputs) for multiphysics couplings. The second term describes the diffusive transport, accounting for the interaction between the dilute species and the solvent. A

field for the diffusion coefficient is available, and any expression containing other variables such as pressure and temperature can be entered here. The node has a matrix that can be used to describe anisotropic diffusion coefficients. Finally, the term on the right-hand side of eq. S4; represents a source or sink term, typically due to a chemical reaction.

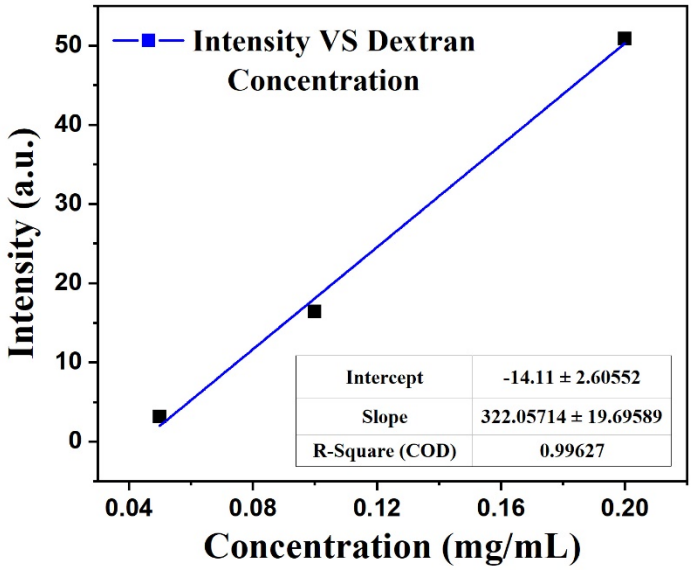

Figure S12. Intensity vs. dextran concentration plot used for calculating permeability values.

Supplementary References

1 O. Y. F. Henry, R. Villenave, M. J. Cronce, W. D. Leineweber, M. A. Benz and D. E. Ingber, *Lab on a Chip*, 2017, **17**, 2264–2271.

2 M. J. C. Santbergen, M. van der Zande, A. Gerssen, H. Bouwmeester and M. W. F. Nielen, *Analytical and Bioanalytical Chemistry*, 2020, **412**, 1111–1122.

3 P. de Haan, M. J. C. Santbergen, M. van der Zande, H. Bouwmeester, M. W. F. Nielen and E. Verpoorte, *Scientific Reports*, 2021, **11**, 1–13.

4 K. Pocock, L. Delon, V. Bala, S. Rao, C. Priest, C. Prestidge and B. Thierry, *ACS Biomaterials Science and Engineering*, 2017, **3**, 951–959.

5 K. Kulthong, L. Duivenvoorde, H. Sun, S. Confederat, J. Wu, B. Spenkelink, L. de Haan, V. Marin, M. van der Zande and H. Bouwmeester, *Toxicology in Vitro*, 2020, **65**, 104815.

6 S. Muenchau, R. Deutsch, T. Hielscher, N. Heber, B. Niesler, M. L. Stanifer and S. Boulant, *bioRxiv*, 2018, **39**, 1–21.

7 K. Y. Shim, D. Lee, J. Han, N. T. Nguyen, S. Park and J. H. Sung, *Biomedical Microdevices*, , DOI:10.1007/s10544-017-0179-y.

8 P. Shah, J. V. Fritz, E. Glaab, M. S. Desai, K. Greenhalgh, A. Frachet, M. Niegowska, M. Estes, C. Jäger, C. Seguin-Devaux, F. Zenhausern and P. Wilmes, *Nature Communications*, , DOI:10.1038/ncomms11535.

9 S. Jalili-Firoozinezhad, F. S. Gazzaniga, E. L. Calamari, D. M. Camacho, C. W. Fadel, A. Bein, B. Swenor, B. Nestor, M. J. Cronce, A. Tovaglieri, O. Levy, K. E. Gregory, D. T. Breault, J. M. S. Cabral, D. L. Kasper, R. Novak and D. E. Ingber, *Nature Biomedical Engineering*, 2019, **3**, 520–531.

10 S. J. Trietsch, E. Naumovska, D. Kurek, M. C. Setyawati, M. K. Vormann, K. J. Wilschut, H. L. Lanz, A. Nicolas, C. P. Ng, J. Joore, S. Kustermann, A. Roth, T. Hankemeier, A. Moisan and P. Vulto, *Nature Communications*, 2017, **8**, 1–7.

11 M. Arrio-Dupont, S. Cribier, G. Foucault, P. F. Devaux and A. D'Albis, *Biophysical Journal*, 1996, **70**, 2327–2332.